The Astrophysical Journal, 927:62 (12pp), 2022 March 1 https://doi.org/10.3847/1538-4357/ac4961

Suprathermal Ion Energy Spectra and Anisotropies near the Heliospheric Current Sheet Crossing Observed by the Parker Solar Probe during Encounter 7

M. I. Desai[1,2], D. G. Mitchell[3], D. J. McComas[4], J. F. Drake[5], T. Phan[6], J. R. Szalay[4], E. C. Roelof[3], J. Giacalone[7], M. E. Hill[3], E. R. Christian[8], N. A. Schwadron[9], R. L. McNutt, Jr.[3], M. E. Wiedenbeck[10], C. Joyce[4], C. M. S. Cohen[10], A. J. Davis[10], S. M. Krimigis[3], R. A. Leske[10], W. H. Matthaeus[11], O. Malandraki[12], R. A. Mewaldt[10], A. Labrador[10], E. C. Stone[10], S. D. Bale[6], J. Verniero[8], A. Rahmati[6], P. Whittlesey[6], R. Livi[6], D. Larson[6], M. Pulupa[6], R. J. MacDowall[8], J. T. Niehof[9], J. C. Kasper[13], and T. S. Horbury[14]
[1] Southwest Research Institute, 6220 Culebra Road, San Antonio, TX 78238, USA
[2] Department of Physics and Astronomy, University of Texas at San Antonio, San Antonio, TX 78249, USA
[3] Johns Hopkins University/Applied Physics Laboratory, Laurel, MD 20723, USA
[4] Department of Astrophysical Sciences, Princeton University, Princeton, NJ 08544, USA
[5] Department of Physics, Institute for Physical Science and Technology, University of Maryland, College Park, MD 20742, USA
[6] Physics Department and Space Sciences Laboratory, University of California, Berkeley, Berkeley, CA 94720, USA
[7] The University of Arizona, Lunar and Planetary Laboratory, Tucson, AZ 85721, USA
[8] NASA Goddard Space Flight Center, Greenbelt, MD 20771, USA
[9] Department of Physics and Astronomy, University of New Hampshire, Durham, NH 03824, USA
[10] Jet Propulsion Laboratory, California Institute of Technology, Pasadena, CA 91125, USA
[11] Department of Physics and Astronomy, University of Delaware, Newark, DE 19716, USA
[12] Institute for Astronomy, Astrophysics, Space Applications & Remote Sensing (IAASARS), National Observatory of Athens, Greece
[13] Climate and Space Sciences and Engineering, University of Michigan, Ann Arbor, MI 48109, USA
[14] Faculty of Natural Sciences, Department of Physics, Imperial College, London, UK
Received 2021 October 25; revised 2021 December 1; accepted 2021 December 10; published 2022 March 4

Abstract

We present observations of $\gtrsim$10–100 keV nucleon^{-1} suprathermal (ST) H, He, O, and Fe ions associated with crossings of the heliospheric current sheet (HCS) at radial distances of <0.1 au from the Sun. Our key findings are as follows: (1) very few heavy ions are detected during the first full crossing, the heavy-ion intensities are reduced during the second partial crossing and peak just after the second crossing; (2) ion arrival times exhibit no velocity dispersion; (3) He pitch-angle distributions track the magnetic field polarity reversal and show up to ∼10:1 anti-sunward, field-aligned flows and beams closer to the HCS that become nearly isotropic farther from the HCS; (4) the He spectrum steepens either side of the HCS, and the He, O, and Fe spectra exhibit power laws of the form $\sim E^{-4}$–E^{6}; and (5) maximum energies E_X increase with the ion's charge-to-mass (Q/M) ratio as $E_X/E_H \propto (Q_X/M_X)^{\delta}$, where $\delta \sim 0.65$–0.76, assuming that the average Q states are similar to those measured in gradual and impulsive solar energetic particle events at 1 au. The absence of velocity dispersion in combination with strong field-aligned anisotropies closer to the HCS appears to rule out solar flares and near-Sun coronal-mass-ejection-driven shocks. These new observations present challenges not only for mechanisms that employ direct parallel electric fields and organize maximum energies according to E/Q but also for local diffusive and magnetic-reconnection-driven acceleration models. Reevaluation of our current understanding of the production and transport of energetic ions is necessary to understand this near-solar, current-sheet-associated population of ST ions.

Unified Astronomy Thesaurus concepts: The Sun (1693); Solar magnetic reconnection (1504); Interplanetary particle acceleration (826); Interplanetary magnetic fields (824); Heliosphere (711)

Supporting material: data behind figure

1. Introduction

Observations over the last two decades have provided compelling evidence that suprathermal (ST) ions in the energy range between ∼1.5 and 2 times the bulk solar wind (SW) energy up to ∼100 keV nucleon^{-1} are an important constituent of the source population that gets accelerated to higher energies via a wide variety of heliospheric phenomena (e.g., see the review by Desai & Giacalone 2016). Examples include coronal-mass-ejection-driven (CME-driven) large gradual solar energetic particle events (LSEPs; Desai et al. 2006), interplanetary (IP) shock-associated energetic storm particle events (ESPs; Desai et al. 2001, 2003), corotating-interaction-region-associated particle events (Mason et al. 2012a; Allen et al. 2019), and Earth's bow shock (e.g., Dwyer et al. 1997; Starkey et al. 2021). With contributions from multiple sources such as the heated SW, impulsive and gradual SEP events, IP shock-associated ESPs, as well as interstellar and inner source pickup ions, the pool of ST material inside 1 au is highly dynamic and varies in time and location (e.g., Mason et al. 2006; Dayeh et al. 2017). Thus, research devoted to understanding the origin and acceleration of ST ions has gained significant importance as it constitutes a key to unlocking details of the physics of particle acceleration throughout the heliosphere and beyond (e.g., Caprioli et al. 2018).

On 2021 January 17, when NASA's Parker Solar Probe (PSP) was close to perihelion at a radial distance of <0.1 au at ∼20 solar radii (R_s) during orbit 7 (E07), the Integrated Science Investigation of the Sun-Energetic Particle-Low energy instrument (IS⊙IS/EPI-

Lo; McComas et al. 2016) observed significant increases in the intensities of <100 keV nucleon^{-1} ST protons and heavy ions, such as He, O, and Fe both before and after two distinct crossings of the heliospheric current sheet (HCS) as identified by the magnetic field and SW plasma instruments. In this paper, we present a detailed analysis of the properties of ST ions associated with this HCS crossing, particularly focusing on He time–intensity profiles, ion arrival times and velocity dispersion, time evolution of He pitch-angle distributions (PADs) and anisotropies, and ion energy spectra and maximum observed energies. We discuss the implications of these results in terms of potential sources, expectations of remote versus local acceleration mechanisms, and existing propagation models of ST ions in the inner heliosphere.

2. Instrumentation and Data Analysis

Since its launch on 2018 August 12, PSP (Fox et al. 2016) has completed its first nine orbits around our Sun and provided unprecedented observations of the inner heliosphere. PSP will use three more Venus flybys to reach within ∼0.04 au (∼9 R_s) of the Sun's surface. PSP carries four instrument suites, namely, (1) the Solar Wind Electrons, Alphas, and Protons Investigation (SWEAP; Kasper et al. 2016); (2) the Electromagnetic Fields Investigation (FIELDS; Bale et al. 2016); (3) IS⊙IS (McComas et al. 2016); and (4) the Wide-field Imager for Solar Probe (Vourlidas et al. 2016). Together these suites provide comprehensive measurements of the in situ SW, the electromagnetic fields, and energetic particles, as well as contextual white-light images of the solar corona and the inner heliosphere.

The IS⊙IS suite comprises two instruments—the low-energy Energetic Particle Instrument—EPI-Lo—and the high-energy Energetic Particle Instrument—EPI-Hi (McComas et al. 2016) that provide detailed measurements of the energy spectra, arrival directions, and composition of H–Fe ions from ∼0.02 up to 200 MeV nucleon^{-1}, as well as of the energy spectra and arrival directions of 0.025–6 MeV electrons (e.g., McComas et al. 2019). We also use supporting data from the FIELDS and SWEAP instrument suites.

In this study, our primary data are taken from the IS⊙IS/EPI-Lo instrument (McComas et al. 2016; Hill et al. 2017). EPI-Lo measures the energy spectra, composition, and arrival directions of ions above ∼0.02 MeV nucleon^{-1} that enter one of its 80 apertures. As the ions pass through the start foils located at the entrance of each aperture, they generate secondary electrons which provide the start time-of-flight (ToF) signal. The ions then strike a stop foil where they generate secondary electrons for the stop ToF signal. Above specific energies for each species, a solid-state detector (SSD) directly behind the stop foil also measures the residual kinetic energy (E) of the ion. The coincidence between start, stop, and energy signals provide triple-coincidence measurements, and the measured ToF and E are used to identify the species. All valid triple-coincidence ion events are binned according to the identified species in pre-defined incident energy ranges by onboard lookup tables based on pre-flight calibration data (see McComas et al. 2016) and on the instrument response during the 2020 November CME-associated SEP/ESP event when count rates for all species were sufficiently high to populate the corresponding tracks in the ToF versus E matrix (see M. E. Hill et al. 2021, in preparation). In this study we use the binned "ion composition" ToF versus E and the raw triple-coincidence H, He, O, and Fe data directly from the ToF versus E matrices for characterizing the properties of ST ions associated with the HCS crossing.

3. Observations

3.1. Overview and Time Histories

Figure 1 provides an overview of the IS⊙IS, SWEAP, and FIELDS observations during the 18 hr interval starting from 0600 UT on 2021 January 17 and ending at 0000 UT on 2021 January 18. During this period, IS⊙IS observed a population of dispersionless ST ions (i.e., simultaneous intensity increases at all measured energies) that is likely associated with the crossing of the HCS at ∼1340 UT on 2021 January 17. The figure shows the (a) ∼15–90 keV nucleon^{-1} H, He, O, and Fe omnidirectional intensities, (b) ∼30–85 keV nucleon^{-1} He omnidirectional intensities in three different energy ranges, (c) ∼30–90 keV nucleon^{-1} He spectral slope, (d) 1/ion speed spectrograms constructed using the ToF versus E counts for all species, (e) ∼35–70 keV nucleon^{-1} He PADs, (f) ∼253–314 eV electron PADs—the field-aligned electron strahl—measured by SWEAP, (g) bulk SW speed, and (h) the interplanetary magnetic field or IMF magnitude $\boldsymbol{B}$ and (i) its radial component $\boldsymbol{B}_R$. Blue vertical lines identify the following five time intervals, as identified from the FIELDS and SWEAP data: (1) prior to the first crossing, (2) during the first full crossing, (3) in between the two crossings, (4) during the second partial crossing, and (5) after the second crossing. These different regions can also be seen from $\boldsymbol{B}$ and $\boldsymbol{B}_R$ in Figures 1(h) and (i), respectively.

Figures 1(a) and (b) show that IS⊙IS/EPI-Lo observed significant increases in <100 keV nucleon^{-1} H, He, O, and Fe intensities both before and after the two HCS crossings. Very few heavy ions are detected during the first full crossing while the intensities are reduced during the second partial crossing. The He intensities peak just after the magnetic field polarity reversal associated with the second partial crossing, as seen in Figure 1(i). Figure 1(c) shows that the He spectral slope varies between ∼4 and 8 before the first full crossing and remains relatively constant at ∼6 after the second HCS crossing (i.e., during the peak intensity enhancement seen in Figures 1(a) and (b)). Figures 1(e) and (f) show that the ST He and the electron PADs track the magnetic field polarity reversal associated with the HCS. In particular, prior to the HCS crossing, $B_R > 0$ and both the ST He PADs and the strahl peak at PA's between ∼0° and 45°, while after the HCS crossing, $B_R < 0$ and the He PADs and the strahl peak at PA's between ∼135° and 180°. This indicates that during these intervals, both the ST He ions and the strahl electrons are flowing away from the Sun and along the interplanetary magnetic field lines. It is interesting that the strahl broadens in pitch angle from 30° to >50° during the ∼3 hr before and after the HCS crossings in conjunction with the observed increases in the ST ion intensities shown in Figures 1(a) and (b). Although the strahl intensity decreases it does not completely drop out during the ST ion intensity enhancements in between the HCS crossings, indicating that those field lines are still connected to the Sun. Figure 1(d) reveals a clear lack of velocity dispersion during the onsets of individual intensity enhancements seen in Figures 1(a) and (b).

To examine the temporal evolution of the PADs and the heavy-ion energy spectra, we separate out the time intervals prior to the first crossing and after the second crossing each into two shorter time intervals that represent regions traversed by

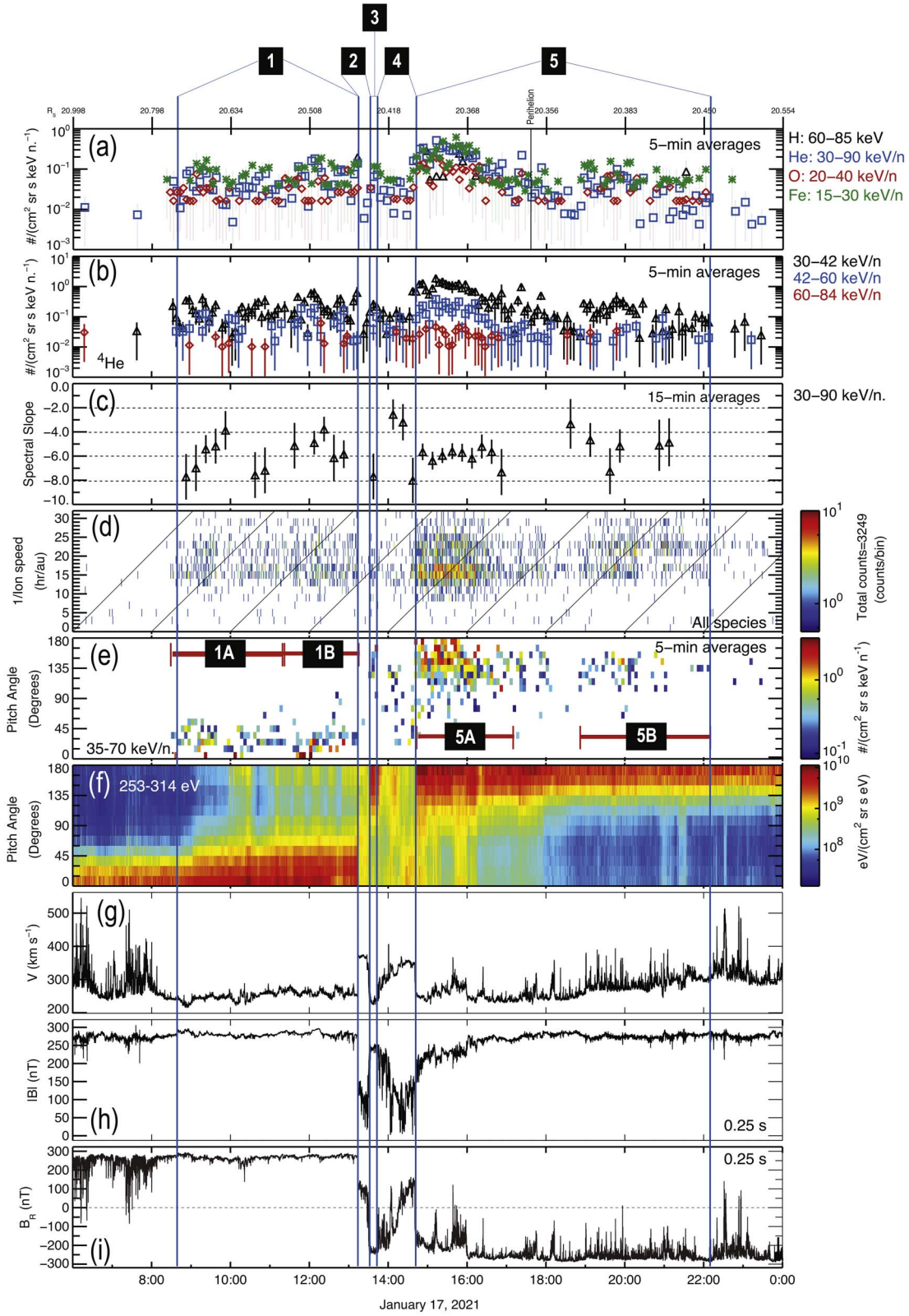

Figure 1. (a) 5 minute averages of ∼15–90 keV nucleon^{-1} H, He, O and Fe intensities, (b) 5 minute averages of ∼30–85 keV nucleon^{-1} He intensities, (c) 15 minute averages of ∼30–90 keV nucleon^{-1} He spectral slope, (d) 1 minute averages of the 1/ion speed spectrograms constructed from all valid triple-coincidence ion counts (ToF vs. *E*) detected by EPI-Lo, (e) 5 minute averages of the ∼35–70 keV nucleon^{-1} He pitch-angle distributions (PADs) in the spacecraft frame, (f) 0.87 s averages of ∼253–314 eV electron PADs, (g) ∼3.5 s average of the bulk solar wind speed, and (h) ∼0.25 s averages of magnetic field magnitude, and (i) the radial component of the magnetic field in the Sun-centered RTN coordinate system. The black vertical bar in (a) shows PSP perihelion. Vertical blue bars: time intervals identified as (1) prior to first crossing, (2) during the first crossing, (3) in between two crossings, (4) second partial crossing, and (5) after second crossing. Time periods 1A, 1B, 5A, and 5B in (e) identify time intervals selected for analyses of PADs and energy spectra (see the text for details).

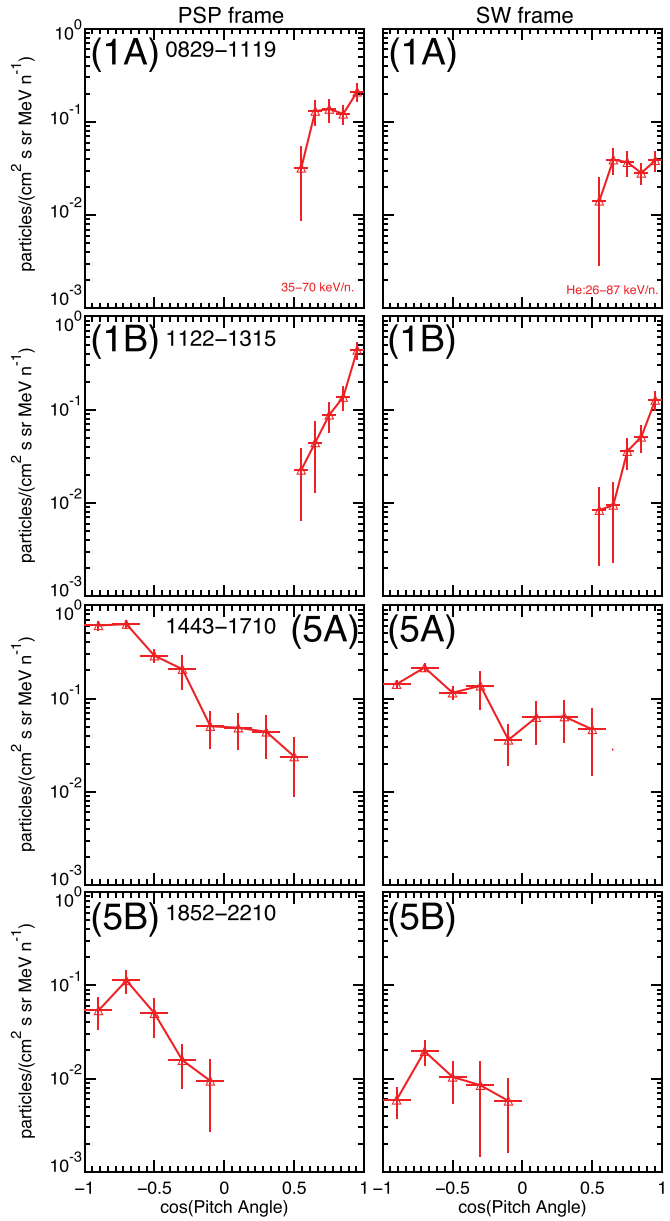

Figure 2. PADs plotted as differential intensity vs. cosine of the PAs averaged during the four time intervals identified in Figure 1(e). Left: PADs in spacecraft frame. Right: PADs transformed into the bulk solar wind plasma frame.

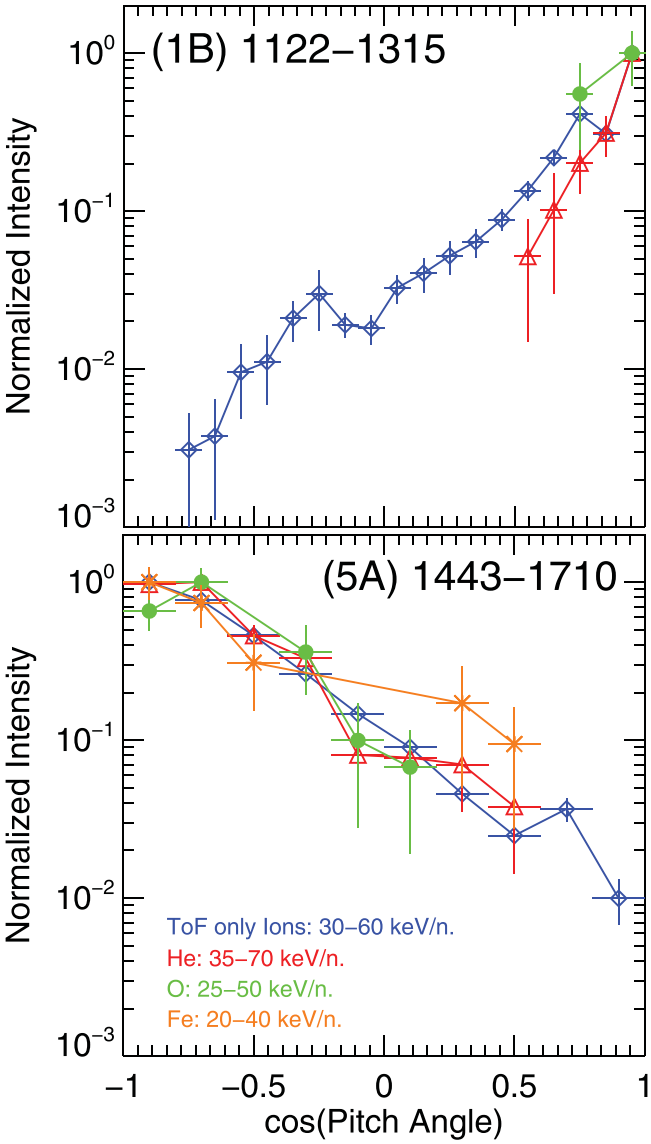

Figure 3. Normalized intensity vs. cosine of the PAs in the spacecraft frame averaged during two of the time intervals, 1B and 5A, identified in Figure 1(e). The intensities for each species are normalized to the corresponding maximum intensity during the interval.

PSP further away from the HCS (intervals 1A and 5B) and regions closer to the HCS (intervals 1B and 5A). These sampling intervals are chosen somewhat subjectively and correspond roughly to the discrete ST ion intensity increases seen in Figures 1(a) and (b). We remark that the overall behavior of the PADs and the energy spectra shown in Figures 2–4 does not change even if these time intervals are shortened or lengthened.

3.2. Pitch-angle Distributions

EPI-Lo has 80 apertures that sample a wide range of pitch angles (PAs) over a hemisphere during any given time interval (McComas et al. 2016; Hill et al. 2017). However, because of changes in the direction of the magnetic field, this coverage is neither uniform and only rarely does it sample the full (180°) range of PAs all the time, and so we must exercise caution when interpreting the PADs. For example, the lack of intensity enhancements during interval 4 at PAs between 140° and 180° is partly due to the lack of coverage at these PAs during a large fraction of the time interval, which results in more than an order of magnitude (not shown) difference in the number of EPI-Lo apertures that sampled PAs between 100° and 140°. Figure 2 shows the PADs, plotted as differential intensity versus the cosine of the PAs in the four intervals described in Figure 1(e). Only data points with at least one count are shown. The left panels show the PADs in the spacecraft (SC) frame, while the right panels show the corresponding distributions transformed into the bulk SW plasma frame using the anisotropic Compton–Getting transformation techniques described in the literature (see Ipavich 1974; Sanderson et al. 1985; Stevens & Hoyng 1986; Alevizos et al. 1999; Dalla & Balogh 2001; Lario et al. 2005). Note that the energy ranges in the two frames are different because of the Compton–Getting effect, due to which ions measured in a given energy range in the sunward-facing apertures i.e., those apertures

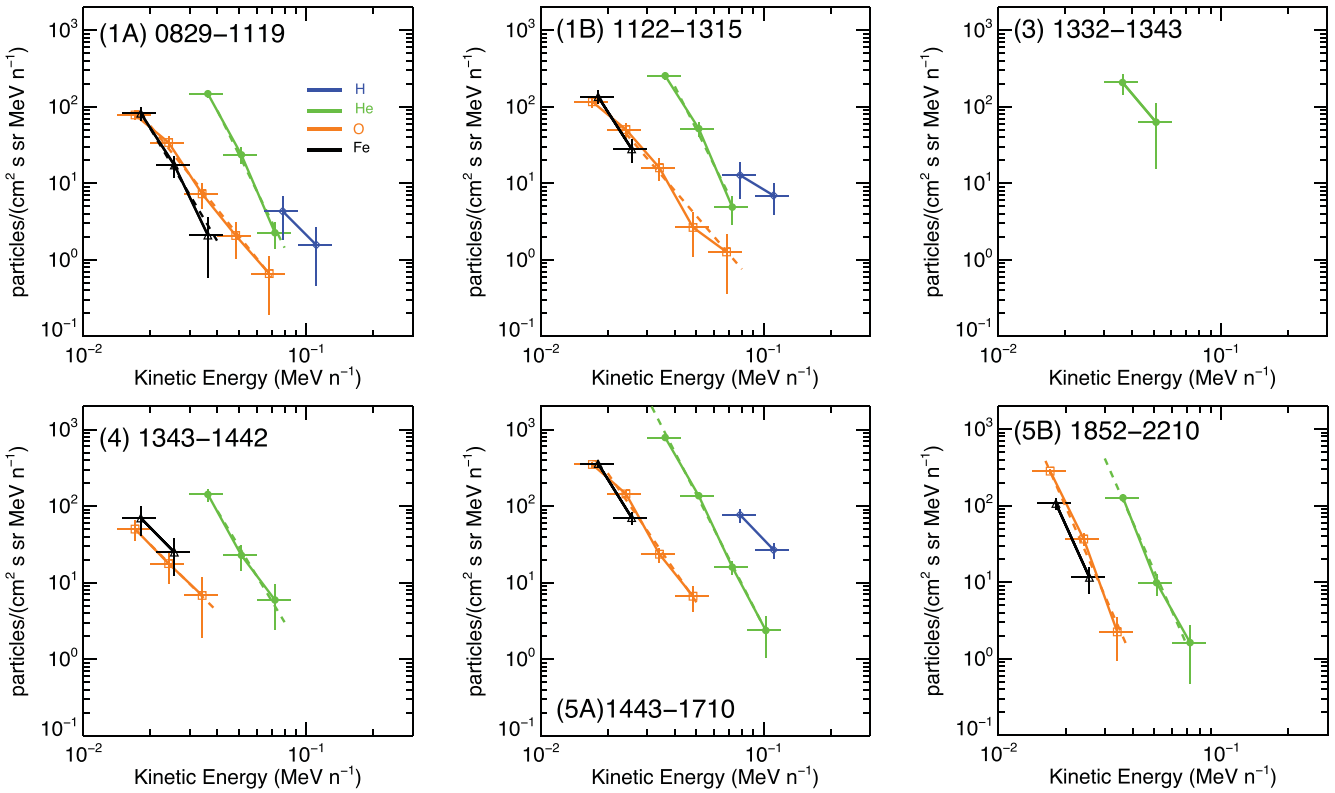

Figure 4. Differential energy spectra for H, He, O, and Fe in six different time intervals associated with the HCS crossing (see Figure 1). Dashed lines represent power-law fits to the He (green), O (orange), and Fe (black) spectra, with the power-law spectral indices provided in Table 1.

with viewing directions opposite to the solar wind flow vector, have lower energies in the SW frame, while those measured in the same energy range in opposite-facing apertures have higher energies in the SW frame. The data in the 1/ion speed spectrograms in Figure 1(d) and the He PADs in the right panels of Figure 2 are plotted after subtracting the nonnegligible PSP velocity vector from the measured ion velocity.

Figure 2 shows the following: (1A) farther away from the HCS and prior to the first full crossing, the PADs show anti-sunward, field-aligned flow in the PSP frame but become nearly flat when transformed into the plasma frame. (1B) Closer to the HCS, the PADs in both frames show ∼10:1 anti-sunward, field-aligned anisotropies that point to field-aligned beam-like distributions. (5A) After the second crossing and closer to the HCS, the PADs show a smaller (but still ∼5:1) anisotropy in the SW frame compared with the PSP frame (as expected from the Compton–Getting transformation of a steep spectrum). Owing to the significantly stronger dependence of the intensity as a function of PA in the sunward hemisphere, we consider that the SW frame PADs prior to the HCS crossing in Figure 2: 1B exhibit a more beam-like distribution compared with that seen after the HCS crossing in Figure 2: 5A, which is more typical of field-aligned flows. (5B) Far away from the HCS after the second crossing, the PADs in the PSP frame show an anti-sunward, field-aligned flow that peaks at ∼−0.75 or at PAs of ∼20°–40°, which is partly due to the uneven and nonuniform PA sampling and coverage discussed above. Like the PADs seen well before the HCS crossing in Figure 2, the PADs observed farther away after the HCS crossing also become nearly flat in the SW frame, which may be a result of stronger PA scattering and a convective, rather than streaming, anisotropy. In summary, the PADs farther away from the HCS are flatter and appear to indicate more isotropic distributions compared with those seen closer to the HCS crossing.

To investigate the species dependence of the PADs, we plot in Figure 3 the SC-frame-normalized intensity versus cosine of the PAs for He, O, and Fe ions as well as for double-coincidence ToF-only ions, which are likely to be dominated by protons (e.g., see McComas et al. 2019), during the two time intervals identified as 1B and 5A in Figure 1(e). As shown in Figure 2, however, we did not transform these PADs into the SW frame because Compton–Getting transformation of the Fe and O intensities with lower counting statistics yields relative uncertainties >100% for most data points. The figure clearly shows that the SC-frame PADs for the different species are remarkably similar. This taken together with the similarity in the spectral forms and slopes shown in Figure 4 and Table 1 across overlapping energy ranges for the three species indicates that the SW frame PADs for Fe and O are also likely to have similar characteristics to those seen for He, and hence that the ST heavy-ion anisotropies are independent of species over the energy range EPI-Lo measured statistically significant counts.

3.3. Spectral Properties

Figure 4 shows the H, He, O, and Fe differential energy spectra in six different time intervals. Energy spectra with three or more statistically significant data points with relative uncertainty ⩽100% are fitted with power laws of the form $j = j_0 E^{-\gamma}$. Spectral slopes for energy spectra with only two statistically significant data points are calculated using $\gamma = -\ln(j_1/j_2)/\ln(E_1/E_2)$. These time-resolved spectral slopes and indices, along with the event-averaged values for He, O, and Fe, are provided in Table 1. The figures and the table show that the He, O, and Fe spectra behave as steep power laws with indices and slopes between ∼4–6 ± 0.3/1.2 in all

Table 1
Time-resolved and Event-averaged Spectral Indices of He, O, and Fe Measured by IS⊙IS/EPI-Lo during the E07 HCS Crossing

Species	Energy Range (keV n^{-1})	Spectral Index, γ					Maximum Observed Energies			
		1A: Prior to HCS Crossing 1: 0829–1119	1B: Prior to HCS Crossing 1: 1122–1315	5A; After HCS Crossing 2: 1443–1710	5B: After HCS Crossing 2: 1442–1900	Event Averaged: 0839–2210	E/nucleon (keV n^{-1})	E (keV)	E/Q (keV/Q)[a]	Rigidity (MV)[a]
H	...	...	...	...	...	...	91	91	91	13
^{4}He	30–90	5.94 ± 0.70	5.83 ± 0.74	5.72 ± 0.31	6.62 ± 0.74	6.07 ± 0.33	70	281	140	23
O	15–75	3.63 ± 0.31	3.40 ± 0.37	4.24 ± 0.49	5.90 ± 0.55	4.56 ± 0.21	40	647	105	23
Fe	20–40	4.89 ± 1.18	4.53 ± 1.12	4.69 ± 0.63	6.42 ± 1.20	5.14 ± 0.82	29	1648	156	39

Notes. The different time intervals are identified in Figure 1(d). Maximum incident energy for each species is determined from triple-coincidence events analyzed by IS⊙IS/EPI-Lo from 0839 to 2210 UT on 2021 January 17 (see Figure 4(a)).

[a] E/Q and ion rigidity, R, are estimated using average ionization states measured between ∼0.18 and 0.24MeV nucleon^{-1} in large gradual solar energetic particle events (LSEPs) at 1 au (Klecker et al. 2007, p. 273).

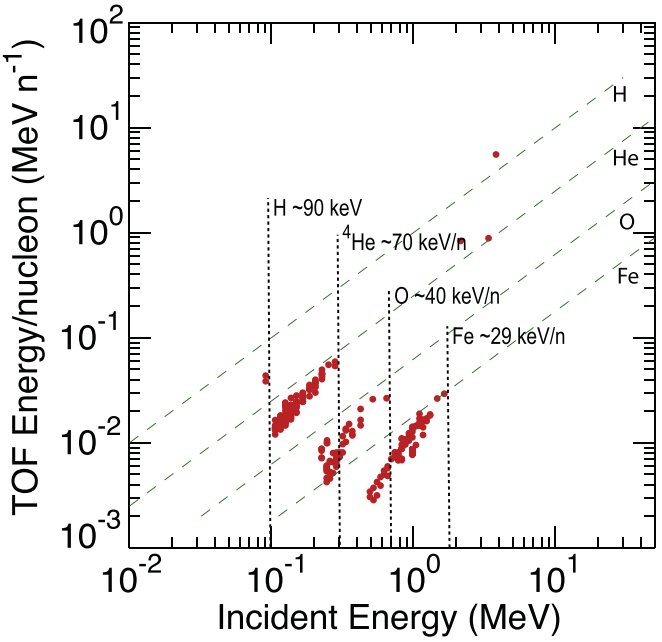

Figure 5. Energy/nucleon (MeV nucleon^{-1}) estimated from the time-of-flight (ToF) measurement vs. the total incident energy (MeV) of all triple-coincidence H, He, O and Fe events identified by IS⊙IS/EPI-Lo from 0839 to 2210 UT on 2021 January 17. The ToF energy/nucleon is determined from the ion speed or ToF measurement and the total incident energy is estimated from the residual energy deposited in the SSD after accounting for energy losses in the start and stop foils, the SSD dead layer, and pulse height defect (see M. E. Hill et al. 2021, in preparation). Green diagonal lines show the location of the H, He, O, and Fe tracks as determined from similar raw event data obtained during the high count rate 2020 November 20 CME/ESP event. Dotted vertical lines show the maximum incident energy for each species, as determined from the corresponding total incident energy.

(The data used to create this figure are available.)

time intervals. In the two intervals prior to the HCS crossing, the O and Fe spectra appear to be somewhat harder than the He spectra. However, just after the second crossing when the ST ion intensities reached their peaks (see Figures 1(a), (b)) and also when averaged over the entire event, the spectral indices for the three species are similar within the uncertainties, with the species-averaged value being $\sim 5.26 \pm 0.76$, which is consistent with a steep velocity phase-space distribution function $f \propto v^{-12.5}$. Thus, it is plausible that the >10 keV nucleon^{-1} ST ions seen near the E07 HCS crossing constitute the tail of the heated and accelerated SW distributions, as suggested by Kasper et al. (2017) and shown in Bale et al. (2021).

3.4. Maximum Observed Energy

In order to estimate the maximum energy for each species, we examine the raw triple-coincidence event data from 0839 to 2210 UT on 2021 January 17. Figure 5 shows the energy nucleon^{-1} calculated from the ion speed measured by the start and stop ToF signals plotted versus the total incident energy for all raw events that were identified as H, He, O, or Fe. The total incident energy is the characteristic energy of the bin that a particular event is assigned to by the onboard lookup tables. The energy bin assignment is determined after estimating energy losses in the start and stop foils, the SSD dead layer, and pulse height defect, and thus represents the best available estimate for the ion's incident energy. The green diagonal lines represent species tracks that were well defined and populated during the 2020 November 25 SEP event (see M. E. Hill et al. 2021, in preparation). The maximum observed energies for each species as determined from these triple-coincidence event data are shown as vertical dotted lines and provided in Table 1 as energy nucleon^{-1}, total energy, energy/charge, and particle rigidity. For the calculation of energy/charge and rigidity, we assume average ionization states for O6.15+ and Fe10.6+ measured in large gradual SEPs at 1 au between ~0.18 and 0.24 MeV nucleon^{-1} (Klecker et al. 2006a, 2006b, 2007, p. 273). Figure 5 and Table 1 clearly show that these four species do not share a common maximum total energy, energy/nucleon, energy/charge, or rigidity.

4. Discussion

During encounter 07 near perihelion at 0.095 au, PSP crossed the HCS at 1340 UT on 2021 January 17. FIELDS and SWEAP detected anti-sunward-directed reconnection exhausts, indicating that the corresponding reconnection X-line is located sunward of PSP (Phan et al. 2021b). Key IS⊙IS observations during this HCS crossing are as follows:

1. EPI-Lo observed significant increases in >10–100 keV nucleon^{-1} He, O, and Fe intensities in the separatrices before and after the two HCS crossings, with the peak occurring just after IMF polarity reversal associated with the second partial crossing. Interestingly, very few heavy ions are detected inside the first full HCS crossing, and the heavy-ion intensities are significantly reduced during the second partial crossing.
2. The intensity onsets or peaks exhibit no clear velocity dispersion and occur in conjunction with a persistent, anti-sunward strahl that broadens in PAs from 30° to >50°.
3. The He PADs when transformed into the bulk plasma frame, like the strahl, closely track the magnetic field polarity reversal associated with the HCS and show up to ~10:1 anti-sunward, field-aligned beams and/or flows closer to the HCS, but are essentially flat farther away, thus indicating the presence of nearly isotropic distributions.
4. The He, O, and Fe spectra behave as steep power laws with E^{-4}–E^{6} before and after the HCS crossing, with each species exhibiting a different maximum incident energy (total energy, energy/nucleon, energy/charge, and rigidity).

We now discuss the implications of these results in terms of local versus remote sources and traditional diffusive versus reconnection-driven particle acceleration models. For the purpose of this discussion, we distinguish between remote or near-solar sources versus relatively local sources, defined here as those within ~1 R_s of the PSP location. These new PSP observations, as summarized in Table 2 and discussed below, raise several important questions about the origin, acceleration, and propagation of ST ions around the HCS inside 0.1 au.

4.1. Velocity Dispersion, PADs, and Local versus Remote Acceleration

The lack of clear velocity dispersion within the 1 minute time resolution of the 1/ion speed spectrograms in Figure 1(d) along with the absence of concomitant flares or near-Sun CME shocks on 2021 January 17, as reported by Earth-based solar

Table 2
Qualitative Comparison between Key IS⊙IS Observations during the 2021 January 17 Heliospheric Current Sheet Crossing Event and Model/Theoretical Predictions

PSP/ISOIS/EPI-Lo Observations	Properties/Implications	Local		Remote	
		Diffusive Models	Reconnection Models	Flare or CME-associated	Direct $E_{\parallel}$ Acceleration
Intensity peaks occur near the HCS crossings but outside the reconnection exhausts	No association with local shocks, compression regions, or visible solar activity	✓	X	X	✓
No velocity Dispersion	Combined with the time evolution of PADs, most likely points to local or nearby sources	✓	✓	X	X
Isotropic PADs far away from HCS crossings	Strong PA scattering, convective anisotropy	✓	?	X	?
Up to ∼10:1 anti-sunward, field-aligned beams and flows closer to the HCS crossings	Weak PA scattering with direct connection to the source region sunward of PSP	X	✓	✓	✓
Spectra are steep power laws with $j \propto E^{-5.26\pm0.76}$	Maxwellian-like phase-space density distribution with $f \propto v^{-12.5}$. Possible ST tail of SW distribution.	?	✓	✓	✓
Maximum Observed Energy E_X for species X	Not ordered by E, E/nucleon, E/Q, or R. $E_X/E_H \propto (Q_X/M_X)^{0.65-0.76}$	✓	✓	✓	X

observatories (see https://solen.info/solar/old_reports/2021/january/20210118.html), rules out the possibility that these ST ions are accelerated and simultaneously injected over a range of energies by near-solar sources but instead points to one of three possibilities: (1) PSP entered flux tubes filled with ST ions that were accelerated remotely (e.g., Mazur et al. 2000), (2) ST ions are being accelerated by unidentified remote sources that inject ions continuously or in a quasi-steady manner, or (3) ST ions are being continuously accelerated at local or nearby sources located within ~1 R_s of PSP. The presence of anisotropic PADs with field-aligned beams and flows closer to the HCS crossings indicates weak PA scattering and is somewhat difficult to reconcile with the notion that PSP entered flux tubes that are filled with remotely accelerated ST ions because typically such populations tend to exhibit nearly isotropic PADs (e.g., Cohen et al. 2020; Desai et al. 2020).

The temporal evolution of the He PADs observed on either side of the HCS crossing also appears to be inconsistent with a remote or solar origin because ion anisotropies in SEP events accelerated in flares or by near-Sun CME-driven shocks tend to exhibit strong anti-sunward flows during their onsets and become more isotropic later when the intensities peak, presumably due to PA scattering and/or diffusive transport (e.g., Kallenrode & Wibberenz 1997; Lario et al. 2005; Giacalone et al. 2020; Mason et al. 2021; Mitchell et al. 2020). In contrast, we find nearly isotropic distributions at the start and the end of the event, which indicates relatively strong PA scattering or diffusive transport farther away from the HCS, while strong (~10:1) anti-sunward beam-like distributions are observed just before the first crossing and anti-sunward flows just after the second crossing. Thus, the time evolution of the PADs is remarkably different from the behavior that is seen routinely during solar or remote origin ion events, and this in combination with the absence of velocity dispersion makes it highly unlikely that these HCS-associated ST ions are continuously injected by near-solar sources (i.e., scenario 2). Instead, this behavior indicates that PSP is probably traversing regions with magnetic field lines directly connected to nearby acceleration sites located sunward of PSP.

Because scenario (3) is plausible, we estimate the possible location of local sources of these ST ions as follows. The observed minimum and maximum ion energies (in energy per nucleon) are ~9.4 keV nucleon^{-1} for Fe and ~91 keV for protons, which correspond to minimum and maximum speeds of ~1345 km s^{-1} and ~4200 km s^{-1}, respectively. Thus, in 60 s, the lowest speed Fe ions could travel from sources located less than ~80,000 km away, while the higher energy protons travel this distance in 19 s, possibly resulting in the observed lack of velocity dispersion. The anti-sunward flows and beams seen in the He PADs suggest that these sources are likely located sunward of PSP, while the persistence of the strahl indicates that the ST ions are injected on field lines that are still connected to the Sun. We remark that Phan et al. (2012b) studied the FIELDS and SWEAP observations associated with the HCS crossings during E07 and E08 in detail. During both crossings, they find strong evidence for magnetic reconnection and the presence of jets with positive radial outflow (ΔV_R). This indicates that the anti-sunward-directed exhausts detected during both E07 and E08 HCS crossings originated from corresponding reconnection X-lines located sunward of PSP. Additionally, Phan et al. (2012b) estimated that the reconnection X-line is at least ~43,000 km sunward of PSP during the E07 HCS crossing, which could serve as a candidate acceleration site/source for the <100 keV nucleon^{-1} H, He, O, and Fe ions seen during the event (see Section 4.3).

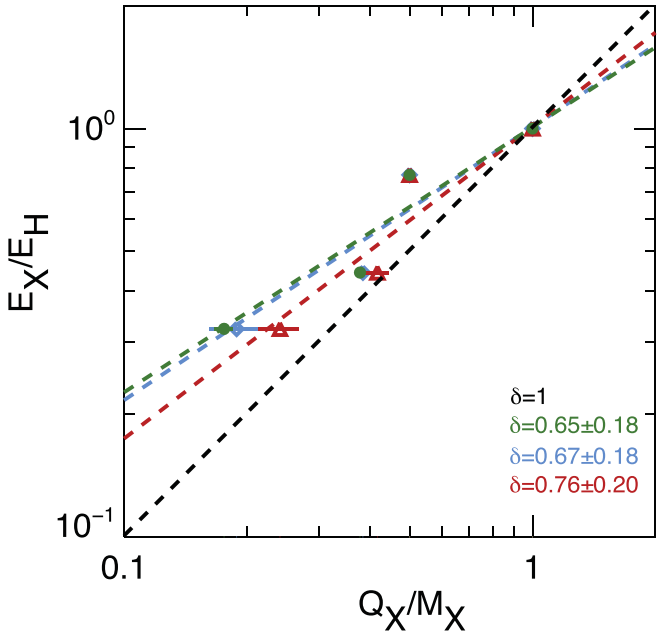

Figure 6. Maximum observed energy E_X vs. ion charge-to-mass ratio for that species. O and Fe ionization states are assumed to be event-averaged charges states measured in the solar wind (green), impulsive (red), and gradual (blue) SEPs. Colored dashed lines represent the corresponding fits to $E_X/E_H \propto (Q_X/M_X)^{\delta}$; the dashed black line represents $E_X/E_H \propto (Q_X/M_X)$, i.e., $\delta = 1$.

4.2. Maximum Energy, PADs, and Diffusive- or E$_{||}$-based Acceleration Processes

Cohen et al. (2005), Mason et al. (2012b), and Desai et al. (2016a, 2016b) showed that the energy dependence of heavy-ion abundances, time evolution of Fe/O ratios, heavy-ion spectral breaks, and other key SEP properties can be explained in terms of a resonance condition where different heavy-ion species, X, have the same parallel diffusion coefficient $\kappa_{\parallel}$ (see Li et al. 2009). Using $\kappa_{\parallel} = \frac{1}{3} v \lambda_{\parallel}$, $\lambda_{\parallel} \propto \left(\frac{Mv}{Q}\right)^{\beta}$, and $E_T = \frac{1}{2} M v^2$, it follows that $\kappa_{\parallel} \sim \left(\frac{M}{Q}\right)^{\beta} E^{\frac{1+\beta}{2}}$, which gives $E_X/E_H \propto (Q_X/M_X)^{\delta}$, where $\delta = 2\beta/(\beta + 1)$. Here E_T and E are the ion's total energy and energy per nucleon, respectively, v is ion speed, $\lambda_{\parallel}$ is the ion's parallel mean free path, and M and Q are the ion's mass and ionization state, respectively. Under this condition, the maximum energies E_X for different species when normalized to the maximum proton energy E_H scale as a power law with the ion's Q_X/M_X ratio. Using the maximum observed energies (E_X in energy/nucleon) for each species X from Figure 5 and Table 1, Figure 6 plots E_X/E_H versus Q_X/M_X assuming average ionization states measured at 1 au in impulsive SEPs between ~0.011 and 0.06 MeV nucleon^{-1} ($O^{6.67+}$ and $Fe^{13.45+}$; DiFabio et al. 2008), in gradual SEPs between ~0.18 and 0.24 MeV nucleon^{-1} ($O^{6.15+}$ and $Fe^{10.6+}$; Klecker et al. 2006a, 2006b, 2007, p. 273) and in the SW ($O^{6.05+}$ and $Fe^{9.84+}$; von Steiger et al. 2000). This figure clearly shows that E_X/E_H is indeed organized by a power law of the form $(Q/M)^{\delta}$, where $\delta \sim 0.66$–0.76.

The fact that each species exhibits different maximum incident energies (total energy, energy/nucleon, energy/charge, and rigidity), particularly when considering the

energy/charge also presents serious challenges for mechanisms that employ direct parallel electric fields ($E_{//}$), such as the so-called pressure cooker mechanism (e.g., Mitchell et al. 2020). It is worth noting that differences in the maximum energy for protons (~91 keV) and He (~140 keV/Q) essentially rule out a common maximum E/Q for all species during this event. This can also be seen from the significant departure of the data points from the dashed black line in Figure 6 which represents $\delta = 1$, i.e., the case where different species have the same maximum energy/charge as protons. The figure illustrates that O and Fe can potentially have the same maximum E/Q as either protons or He, but not both, and that too only if there exists a highly unlikely combination of ionization states, e.g., same E/Q as protons requires $Fe^{18.1+}$ and $O^{7.1+}$, while the same E/Q as He requires $Fe^{11.8+}$ and $O^{4.63+}$. Both combinations correspond to coronal equilibrium temperatures that are more than an order of magnitude different and would essentially require that the two species originate from distinct source regions (Mazzotta et al. 1998; Mason et al. 2016), which is inconsistent with the similarities in the H, He, O, and Fe time–intensity profiles shown in Figures 1(a) and (b), the SC-frame PADs shown in Figure 3, the power-law spectral forms shown in Figure 4, and the corresponding spectral indices listed in Table 1.

While the organization of the maximum energies with Q/M appears to hint at a resonant diffusive-type acceleration mechanism, we note that the presence of up to ~10:1 anti-sunward field-aligned beams and flows indicates weak PA scattering closer to the HCS. Two possibilities could account for this behavior, namely, (1) the observed ion beams/flows closer to the HCS are due to acceleration processes that generate anisotropic distributions at the source region or (2) the PADs are isotropic at the source region and transport effects are responsible for the anisotropies seen at PSP.

We remark that existing theoretical treatments based on first-order Fermi-type diffusive acceleration mechanisms produce nearly isotropic PADs (e.g., Zank et al. 2014; le Roux et al. 2015; Du et al. 2018; Li et al. 2019; Pezzi et al. 2021) and are therefore at odds with scenario (1). It is, however, possible that future modeling efforts that include both the isotropic and the first-order anisotropy in the distribution function could account for the strong ST ion beams/flows shown here. In scenario (2), the stronger anisotropies closer to the HCS crossing could be the result of PSP crossing magnetic field lines that are connected closer to the source regions while the weaker anisotropies further away from the HCS occur because ST ions from the same source regions travel over longer distances, possibly leading to more PA scattering. However, as discussed in Section 4.1, the lack of velocity dispersion points to sources located less than ~10^6 km away, which is significantly smaller than the typically inferred particle mean free paths of $\gtrsim$0.01 au (e.g., Bieber et al. 1994). This implies that the flatter or nearly isotropic distributions seen farther away from the HCS may be difficult to reconcile with existing models of energetic particle transport in solar wind turbulence without invoking an unusually large amount of cross-field diffusion (Dröge 2003; He & Wan 2013; Chhibber et al. 2017). In summary, it appears that existing diffusion-based models of particle acceleration and transport are unable to account for the temporal behavior of the ST ion anisotropies observed in association with the E07 HCS crossing by PSP.

4.3. Maximum Energy and Scale Sizes, Energy Spectra, and Magnetic Reconnection

As alluded to in Section 4.1, a potential local acceleration site is the reconnection X-line, which was at least ~43,000 km sunward of PSP. In situ observations over the last two decades have identified important signatures in the magnetic field and plasma data that confirm the occurrence of magnetic reconnection in a wide variety of locations such as Earth's magnetotail (e.g., Nagai et al. 1998; Øieroset et al. 2001; Angelopoulos et al. 2008), Earth's magnetopause (Paschmann et al. 1979; Phan et al. 2000, 2021a), the solar wind near 1 au (e.g., Gosling et al. 2005a, 2005b; Phan et al. 2006; Gosling & Phan 2013; Khabarova et al. 2016, 2020; Khabarova & Zank 2017), the solar wind beyond 1 au (Gosling et al. 2006), and more recently, the inner heliosphere traversed by PSP (Lavraud et al. 2020; Phan et al. 2020, 2021a; Froment et al. 2021). Although Khabarova & Zank (2017) and Khabarova et al. (2020) report observations of local in situ reconnection-driven acceleration of energetic ions up to ~5 MeV at the L1 Lagrangian point by the Advanced Composition Explorer, this interpretation is somewhat controversial because the Alfvén speed in the solar wind at 1 au is on the order of ~10 s of km s^{-1}, and hence the magnetic energy available for particle energization is considered to be insufficient for accelerating ions up to ST energies (e.g., Gosling et al. 2005c; Phan et al. 2014). In contrast, around the HCS crossing during E07 from ~0839 to 2210 UT on 2021 January 17, the local Alfvén speed at PSP was ~120 km s^{-1} (Phan et al. 2021b). We remark that while the higher Alfvén speeds during E07, and plausibly in association with a reconnection X-line sunward of PSP, could provide sufficient magnetic energy to heat and accelerate solar wind protons, presently it is not clear whether the energy budget would also be able to simultaneously account for the <100 keV ST tails reported in this paper.

Like diffusive acceleration at compression regions and shocks (e.g., Desai & Giacalone and references therein), reconnection-driven particle acceleration processes are also based on first- or second-order Fermi mechanisms but here the particles gain energy primarily due to the curvature drift from magnetic island contraction or merging (e.g., Drake et al. 2009; Zank et al. 2014; le Roux et al. 2015). For energization to occur, all reconnection-driven acceleration mechanisms require the particle gyroradius $\rho \ll t_{HCS}$, where t_{HCS} is the thickness of the HCS. The HCS width is estimated to be ~40,000 km or ~8500 × d_{ion}, where d_{ion} is the ion inertial length (Phan et al. 2021b). From the maximum energies in Table 1 and the magnetic field magnitude measured by FIELDS before, during, and after the HCS crossing, we estimate a gyroradii range of $677 < \rho < 3045$ km inside the HCS and a range of $157 < \rho < 555$ km outside the HCS. Given that closer to the HCS, most of the ions are field aligned and thus have smaller PAs, these values provide upper limits for ρ. It thus appears that the maximum $\rho < t_{HCS}$, which satisfies the required scale size for reconnection-associated mechanisms to operate. In this case, the organization of the maximum energy with Q/M could be a consequence of the particle energy gain scaling with the ion mass or Q/M ratio until the corresponding gyroradius approaches the relevant scale size and escapes (e.g., Drake et al. 2009; Drake & Swisdak 2012; Arnold et al. 2021), rather than due to a resonant diffusive-type mechanism as found for large SEP events (e.g., Desai et al. 2016b).

Several other IS⊙IS observations also appear to be qualitatively compatible with reconnection-driven mechanisms occurring at the X-line located at least ∼43,000 km sunward of PSP, namely, the lack of clear velocity dispersion during the intensity onsets and peaks, the presence of steep power laws, and the anti-sunward field-aligned beams or flows (e.g., Drake et al. 2009, 2013). Note that the steepness of the He, O, and Fe spectra near the E07 HCS crossing is somewhat at odds with earlier reconnection-driven models based on first-order Fermi or diffusive-type acceleration, which tended to produce harder spectra (e.g., Zank et al. 2014). However, more recently Zhao et al. (2018, 2019a, 2019b) extended the traditional first-order Fermi-type diffusive acceleration model of Zank et al. (2014) to include additional particle escape from the finite acceleration region, Li et al. (2019) numerically solved a diffusive-reconnection acceleration model using real MHD simulations of magnetic reconnection, and Arnold et al. (2021) proposed a solar-flare-associated reconnection-driven first-order Fermi-type acceleration mechanism for electrons. Each model, while using a different approach, may potentially be able to generate steeper power laws with spectral indices between ∼3.5 and 6.5 and therefore account for our observations. However, as mentioned earlier, it does remain to be seen whether such mechanisms have the necessary energy budget to operate in the near-Sun HCS and produce the <100 keV nucleon^{-1} ST ion power-law tails reported here.

Finally, despite the qualitative agreement between expectations of reconnection-driven acceleration models and some of our observations, we remark that the total absence or significant reduction of ion intensities during the two HCS crossings, i.e., within the reconnection jets or exhausts poses a serious challenge for such models, as prior observational studies have shown that the highest-intensity enhancements occur inside the diffusion region as predicted by models (e.g., Øieroset et al. 2002; Drake et al. 2009). Another important and puzzling aspect of these observations is that the ST ion intensities peak in conjunction with the persistent presence and broadening of the strahl on either side of the HCS crossings, i.e., when PSP traversed the separatrices. Because the reconnection X-line is located sunward of PSP, the strahl behavior indicates that these separatrix field lines are still connected to the Sun (see Phan et al. 2021b). The strahl broadening in the separatrices may also indicate that the electrons, and indeed the ST ions, are accelerated at a common, relatively local source that is not necessarily in the immediate vicinity of PSP (see Phan et al. 2021b). Future modeling efforts that include detailed comparisons with data will need to investigate whether reconnection-driven particle energization and release could operate near the HCS in the near-Sun SW and account for the strahl and the ST ions observed just outside the exhausts in the separatrix regions traversed by PSP, as reported in this paper.

5. Summary and Conclusions

In summary, the lack of velocity dispersion and the temporal evolution of the He PADs rule out remote acceleration sites and processes such as flares and near-Sun CME-driven shocks. The fact that the maximum energies for the four ion species do not occur at the same E/Q poses serious challenges for mechanisms that employ direct parallel electric fields. Instead, the maximum energies are $\propto(Q_X/M_X)^{\delta}$, where $\delta \sim 0.7$, which, in turn, points to either a resonant diffusive-type mechanism or mechanisms in which particles gain sufficient energy, increase their gyroradii, and escape from the acceleration region. Among the two candidates for local acceleration, our observations present the most serious challenges for traditional first-order diffusive-type acceleration and transport mechanisms as these tend to produce harder energy spectra and nearly isotropic PADs. Possible sources for the ST ions near the 2021 January 17 HCS crossing may involve contracting magnetic islands near the reconnection X-line located at least ∼43,000 km sunward of PSP. However, currently, even such magnetic-reconnection-based acceleration models are unable to account for the total or near absence of ST ions inside the two HCS crossings that comprise the reconnection jets or exhausts. This highlights the need to reevaluate potential sources of these near-solar, current-sheet-associated ST particles. In conclusion, no single existing model or theory appears to fully account for all of the IS⊙IS/EPI-Lo observations presented in this paper, thus requiring a reexamination of existing theories of ST ion production and transport close to the Sun.

This work was supported by NASA's Parker Solar Probe Mission, contract NNN06AA01C. We thank all the scientists and engineers who have worked hard to make PSP a successful mission, in particular the engineers, scientists, and administrators who designed and built IS⊙IS/EPI-Lo, IS⊙IS/EPI-Hi, FIELDS, and SWEAP instrument suites and support their operations and the scientific analysis of its data. For their contributions to the scientific configuration and instrumental analysis, we owe special thanks to P. Kollmann, J. Peachy, and J. Vandegriff at JHU/APL for EPI-Lo. The IS⊙IS data are available athttp://spp-isois.sr.unh.edu/data_public/ as well as at the NASA Space Physics Data Facility. Work at SwRI is supported in part under NASA grant Nos. 80NSSC20K1815, 80NSSC18K1446, 80NSSC21K0112, 80NSSC20K1255, and 80NSSC21K0971.

ORCID iDs

M. I. Desai https://orcid.org/0000-0002-7318-6008
D. G. Mitchell https://orcid.org/0000-0003-1960-2119
D. J. McComas https://orcid.org/0000-0001-6160-1158
J. F. Drake https://orcid.org/0000-0002-9150-1841
T. Phan https://orcid.org/0000-0002-6924-9408
J. R. Szalay https://orcid.org/0000-0003-2685-9801
E. C. Roelof https://orcid.org/0000-0002-2270-0652
J. Giacalone https://orcid.org/0000-0002-0850-4233
M. E. Hill https://orcid.org/0000-0002-5674-4936
E. R. Christian https://orcid.org/0000-0003-2134-3937
N. A. Schwadron https://orcid.org/0000-0002-3737-9283
R. L. McNutt, Jr. https://orcid.org/0000-0002-4722-9166
M. E. Wiedenbeck https://orcid.org/0000-0002-2825-3128
C. Joyce https://orcid.org/0000-0002-3841-5020
C. M. S. Cohen https://orcid.org/0000-0002-0978-8127
A. J. Davis https://orcid.org/0000-0002-9922-8915
S. M. Krimigis https://orcid.org/0000-0003-2781-2386
R. A. Leske https://orcid.org/0000-0002-0156-2414
W. H. Matthaeus https://orcid.org/0000-0001-7224-6024
O. Malandraki https://orcid.org/0000-0002-4751-6835
R. A. Mewaldt https://orcid.org/0000-0003-2178-9111
A. Labrador https://orcid.org/0000-0001-9178-5349
S. D. Bale https://orcid.org/0000-0002-1989-3596
J. Verniero https://orcid.org/0000-0003-1138-652X
A. Rahmati https://orcid.org/0000-0003-0519-6498
P. Whittlesey https://orcid.org/0000-0002-7287-5098

R. Livi https://orcid.org/0000-0002-0396-0547
D. Larson https://orcid.org/0000-0001-5030-6030
M. Pulupa https://orcid.org/0000-0002-1573-7457
R. J. MacDowall https://orcid.org/0000-0003-3112-4201
J. T. Niehof https://orcid.org/0000-0001-6286-5809
J. C. Kasper https://orcid.org/0000-0002-7077-930X
T. S. Horbury https://orcid.org/0000-0002-7572-4690

References

Alevizos, A., Polygiannakis, J., Kakouris, A., & Moussas, X. 1999, SoPh, 186, 401
Allen, R. C., Ho, G. C., & Mason, G. M. 2019, ApJ, 883, L10
Angelopoulos, V., McFadden, J. P., Larson, D., et al. 2008, Sci, 321, 931
Arnold, H., Drake, J. F., Swisdak, M., et al. 2021, PhRvL, 126, 135101
Bale, S. D., Goetz, K., & Harvey, P. R. 2016, SSRv, 204, 49
Bale, S. D., Horbury, T. S., Velli, M., et al. 2021, ApJ, 923, 174
Bieber, J. W., Matthaeus, W. H., Smith, C. W., et al. 1994, ApJ, 420, 294
Caprioli, D., Zhang, H., & Spitkovsky, A. 2018, JPlPh, 84, 715840301
Chhibber, R., Subedi, P., Usmanov, A. V., et al. 2017, ApJS, 230, 21
Cohen, C. M. S., Christian, E. R., Cummings, A. C., et al. 2020, ApJS, 246, 20
Cohen, C. M. S., Stone, E. C., Mewaldt, R. A., et al. 2005, JGRA, 110, A9
Dalla, S., & Balogh, A. 2001, SSRv, 97, 253
Dayeh, M. A., Desai, M. I., Mason, G. M., et al. 2017, ApJ, 835, 155
Desai, M. I., & Giacalone, J. 2016, LRSP, 13, 1
Desai, M. I., Mason, G. M., Dayeh, M. A., et al. 2016a, ApJ, 816, 68
Desai, M. I., Mason, G. M., Dayeh, M. A., et al. 2016b, ApJ, 828, 106
Desai, M. I., Mason, G. M., Dwyer, J. R., et al. 2001, ApJL, 553, L89
Desai, M. I., Mason, G. M., Dwyer, J. R., et al. 2003, ApJ, 588, 1149
Desai, M. I., Mason, G. M., Gold, R. E., et al. 2006, ApJ, 649, 470
Desai, M. I., Mitchell, D. G., Szalay, J. R., et al. 2020, ApJS, 246, 56
DiFabio, R., Guo, Z., Mobius, E., et al. 2008, ApJ, 687, 623
Drake, J. F., Cassak, P. A., Shay, M. A., et al. 2009, ApJL, 700, L16
Drake, J. F., & Swisdak, M. 2012, SSRv, 172, 227
Drake, J. F., Swisdak, M., & Fermo, R. 2013, ApJL, 763, L5
Dröge, W. 2003, ApJ, 589, 1027
Du, S., Guo, F., Zank, G. P., et al. 2018, ApJ, 867, 16
Dwyer, J. R., Mason, G. M., Mazur, J. E., & von Rosenvinge, T. T. 1997, GeoRL, 24, 61
Fox, N. J., Velli, M. C., Bale, S. D., et al. 2016, SSRv, 204, 7
Froment, C., Krasnoselskikh, V., Dudok de Wit, T., et al. 2021, A&A, 650, A5
Giacalone, J., Mitchell, D. G., Allen, R. C., et al. 2020, ApJS, 246, 29
Gosling, J. T., McComas, D. J., Skoug, R. M., & Smith, C. W. 2006, ApJ, 644, 613
Gosling, J. T., & Phan, T. D. 2013, ApJL, 763, L39
Gosling, J. T., Skoug, R. M., Haggerty, D. K., & McComas, D. J. 2005c, GeoRL, 32, L14113
Gosling, J. T., Skoug, R. M., McComas, D. J., & Smith, C. W. 2005a, JGRA, 110, A01107
Gosling, J. T., Skoug, R. M., McComas, D. J., & Smith, C. W. 2005b, GeoRL, 32, L05105
He, H.-Q., & Wan, W. 2013, A&A, 557, A57
Hill, M. E., Mitchell, D. G., Andrews, G. B., et al. 2017, JGR, 122, 1513
Ipavich, F. M. 1974, GeoRL, 1, 149
Kallenrode, M.-B., & Wibberenz, G. 1997, JGR, 102, 22311
Kasper, J. C., Abiad, R., Austin, G., et al. 2016, SSRv, 204, 131
Kasper, J. C., Klein, K. G., Weber, T., et al. 2017, ApJ, 849, 126
Khabarova, O., Zharkova, V., Xia, Q., & Malandraki, O. E. 2020, ApJ, 894, L12
Khabarova, O. V., & Zank, G. P. 2017, ApJ, 843, 4
Khabarova, O. V., Zank, G. P., Li, G., et al. 2016, ApJ, 827, 122
Klecker, B., Möbius, E., & Popecki, M. A. 2006a, SSRv, 124, 289
Klecker, B., Möbius, E., Popecki, M. A., et al. 2006b, AdSR, 38, 493
Klecker, B., Möbius, E., & Popecki, M. A. 2007, in The Composition of Matter, ed. R. von Steiger, G. Gloeckler, & G. M. Mason, Vol. 130 (New York: Springer), 273
Lario, D., Decker, R. B., Livi, S., et al. 2005, JGRA, 110, A09S11
Lavraud, B., Fargette, N., Reville, N., et al. 2020, ApJS, 894, L19
le Roux, J. A., Zank, G. P., Webb, G. M., & Khabarova, O. 2015, ApJ, 801, 112
Li, G., Zank, G. P., Verkhoglyadova, O., et al. 2009, ApJ, 702, 998
Li, X., Guo, F., & Li, H. 2019, ApJ, 879, 5
Mason, G. M., Desai, M. I., Cohen, C. M. S., et al. 2006, ApJL, 647, L65
Mason, G. M., Desai, M. I., & Li, G. 2012a, ApJ, 748, L31
Mason, G. M., Ho, G. C., Allen, R. C., et al. 2021, A&A, 656, L1
Mason, G. M., Li, G., Cohen, C. M. S., et al. 2012b, ApJ, 761, 104
Mason, G. M., Nitta, N. V., Wiedenbeck, M. E., & Innes, D. E. 2016, ApJ, 823, 138
Mazur, J. E., Mason, G. M., Dwyer, J. R., et al. 2000, ApJL, 532, L79
Mazzotta, P., Mazzitelli, G., Colafrancesco, S., & Vittorio, N. 1998, A&AS, 133, 403
McComas, D. J., Alexander, N., Angold, N., et al. 2016, SSRv, 204, 187
McComas, D. J., Christian, E. R., Cohen, C. M. S., et al. 2019, Natur, 576, 223
Mitchell, D. G., Giacalone, J., Allen, R. C., et al. 2020, ApJS, 246, 59
Nagai, T., Fujimoto, M., Saito, Y., et al. 1998, JGR, 103, 4419
Øieroset, M., Lin, R. P., Phan, T. D., et al. 2002, PhRvL, 89, 19
Øieroset, M., Phan, T. D., Fujimoto, M., Lin, R. P., & Lepping, R. P. 2001, Natur, 412, 414
Paschmann, G., Papamastorakis, I., Sckopke, N., et al. 1979, Natur, 282, 243
Pezzi, O., Pecora, F., le Roux, J., et al. 2021, SSRv, 217, 39
Phan, T. D., Bale, S. D., Eastwood, J. P., et al. 2020, ApJS, 246, 34
Phan, T. D., Drake, J. F., Shay, M. A., et al. 2014, GeoRL, 41, 7002
Phan, T. D., Gosling, J. T., Davis, M. S., et al. 2006, Natur, 439, 175
Phan, T. D., Kistler, L. M., Klecker, B., et al. 2000, Natur, 404, 848
Phan, T. D., Lavraud, B., Halekas, J. S., et al. 2021a, A&A, 650, A13
Phan, T. D., Verniero, J. L., & Larson, D. 2021b, GeoRL, in press
Sanderson, T. R., Reinhard, R., van Nes, P., & Wenzel, K.-P. 1985, JGR, 90, 19
Starkey, M. J., Fuselier, S. A., Desai, M. I., et al. 2021, ApJ, 913, 112
Stevens, G. A., & Hoyng, P. 1986, A&A, 168, 354
von Steiger, R., Schwadron, N. A., Fisk, L. A., et al. 2000, JGR, 105, 27217
Vourlidas, A., Howard, R. A., Plunkett, S. P., et al. 2016, SSRv, 204, 83
Zank, G. P., le Roux, J. A., Webb, G. M., et al. 2014, ApJ, 797, 28
Zhao, L. L., Zank, G. P., Chen, Y., et al. 2019a, ApJ, 872, 4
Zhao, L. L., Zank, G. P., Hu, Q., et al. 2019b, ApJ, 886, 144
Zhao, L. L., Zank, G. P., Khabarova, O., et al. 2018, ApJL, 864, L34